INTERFACE

royalsocietypublishing.org/journal/rsif

Research

**Cite this article:** Bhar K, Chang B, Virot E, Straker L, Kang H, Paris R, Clanet C, Jung S. 2019 How localized force spreads on elastic contour feathers. *J. R. Soc. Interface* **16**: 20190267.
http://dx.doi.org/10.1098/rsif.2019.0267

Received: 13 April 2019
Accepted: 28 October 2019

**Subject Category:**
Life Sciences–Engineering interface

**Subject Areas:**
biomechanics, biophysics

**Keywords:**
feathers, impact force, diving

**Author for correspondence:**
Sunghwan Jung
e-mail: sunnyjsh@cornell.edu

†These authors contributed equally to this study.

Electronic supplementary material is available online at https://doi.org/10.6084/m9.figshare.c.4723961.

THE ROYAL SOCIETY PUBLISHING

# How localized force spreads on elastic contour feathers

Kinjal Bhar[1,†], Brian Chang[2,3,†], Emmanuel Virot[4,†], Lorian Straker[5], Hosung Kang[2], Romain Paris[6], Christophe Clanet[6] and Sunghwan Jung[1]

[1]Department of Biological and Environmental Engineering, Cornell University, Ithaca, NY 14853, USA
[2]Virginia Tech, Department of Biomedical Engineering and Mechanics, Blacksburg, VA 24061, USA
[3]Department of Biology, Temple University, Philadelphia, PA 19122, USA
[4]John A. Paulson School of Engineering and Applied Sciences, Harvard University, Cambridge, MA 02138, USA
[5]Centro de Biologia Estrutural e Bioimagem - CENABIO, Universidade Federal do Rio de Janeiro, Rio de Janeiro 21941-902, Brazil
[6]École polytechnique, LadHyX, CNRS UMR 7646, 91128 Palaiseau, France

BC, 0000-0002-4548-1800; EV, 0000-0003-1687-4450; LS, 0000-0001-8431-7897; SJ, 0000-0002-1420-7921

Birds can experience localized forces against their bodies due to impact against solid objects (like a branch or another bird) or water (during plunge-dives or landings). In this study, we hypothesize that densely packed contour feathers around the bird body would spread localized impact force while diving and maintaining plumage integrity. To test the hypothesis, we performed experiments with individual feathers and elastic beams, and developed a theoretical model to determine the response of feathers during the dive. First, we used a micro computed tomography scanner to characterize the internal structure of the contour feather from a northern gannet and calculate Young's modulus of feathers sampled from different parts of the body. This value was found to be of the order of $10^9$ Pa for feathers from chest and belly. Second, we model the feathers as elastic beams taking into account their pre-curvature and non-uniform cross-section. Results from our experiments with polycarbonate beams suggest that the interaction of feathers on the skin patch redistributes the force, thereby reducing the impact on any particular area of the skin. Finally, a theoretical model of multiple overlaying feathers is proposed to quantify the spreading of impact force on the skin of the bird body which shows that the pressure on the skin at the impact point can be reduced by as much as three times the pressure if feathers had been absent.

## 1. Introduction

Feathers are known to serve a variety of functions for birds, such as heat insulation [1], sexual selection [2,3] and, of course, flight [4,5]. In terms of aerodynamics, flight feathers are a topic of interest for efficient and quiet flying [6]. On the other hand, some hummingbirds use their tail feathers to produce sounds for courtship [7,8] owing to morphological specializations of these tail feathers [9,10]. However, the bird's body is covered by contour feathers, resolving its body shape and protecting the thin skin from the environment. The hydrophobic properties of feathers help to reduce the contact time of impacting rain droplets, which in turn reduces the loss of heat when it rains [11]. Feathers also show resistance to water penetration under hydrostatic pressures, which helps aquatic birds remain dry when diving underwater [12,13]. Thus, the maintenance of the plumage's continuous surface is highly important for survival because it protects the body from thermal and mechanical stresses.

Plunge-diving is a highly specialized foraging behaviour observed in a number of bird species. Among them, the northern gannet (*Morus bassanus*) is an extreme plunge-diver, capable of diving at speeds up to 24 m $s^{-1}$ and reaching fish at depths between 10 and 20 m [14,15]. Plunge-diving birds fly or hover high in the air before free-falling towards the water. The initial height before the free

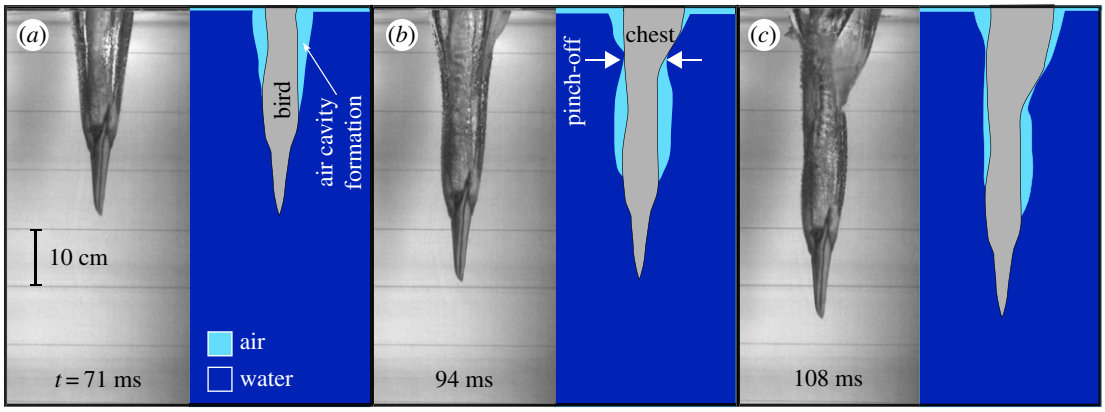


**Figure 1.** High-speed images of a salvaged, frozen northern gannet impacting water at approximately 4.7 m $s^{-1}$ [17]. The moment the beak touches the water marks $t = 0$ ms (not shown) and the beginning of the impact phase. (*a*) The air cavity phase, (*b*) the moment of pinch-off and (*c*) the submerged phase. (Online version in colour.)

fall depends on the depth of prey and the type of prey the bird is after. During head-first free-fall, the bird will accelerate due to gravity and hit the water at high speed; if fast enough it will surprise the prey not giving it a chance to escape.

There are three notable phases during a plunge-dive: (1) the impact phase, (2) the air cavity phase and (3) the submerged phase [16]. It was shown during the impact and air cavity phase that the bird's neck is at greater risk of injury [17]. While northern gannets typically dive at around 24 m $s^{-1}$ in nature [14], their hypothetical maximum diving speed would be up to 80 m $s^{-1}$ before neck injuries due to the morphological properties of the skull and strength of neck muscles [17]. Near the end of the second phase, the air cavity closes, or pinches off, and the bird's upper chest at the shoulder girdle hits water at high speeds (figure 1). This hydrodynamic impact force is highly localized at the upper-chest and makes it a potential danger for the bird. However, due to the elastic coupling of multiple contour feathers, we hypothesize that the force is spread along the feather pattern, over a much larger area of the body, before being transferred to the skin thus reducing pressure on skin after pinch-off.

Contour feathers make up the plumage around the bird's body and could serve a variety of purposes. The elastic property of individual feathers has been studied experimentally [18–26] though few studies have focused on contour feathers [27,28]. However, the interactions among a collective group of feathers remain unknown. When one contour feather is subjected to a force, the other neighbouring feathers will be also affected through a mechanical interaction between feathers in a cascading effect. Such a collective behaviour cannot be deduced from the simple behaviour of a single feather.

Bird feathers are composed of $\beta$-keratin [29], which is a protein in a stacked-sheet configuration. However, the reported values of bird feather elastic modulii have a large range (from lowest value at approx. 0.045 GPa [30] to the largest values of approx. 10 GPa [18]) despite their similar chemical composition. A variety of factors are associated with this range of values, such as method of testing [18,24,31,32], bird species [19], feather type (contour, wing, tail) and moisture content [33]. In order to understand how multiple feathers interact with each other, one must set the groundwork for the mechanical behaviour and elastic modulus of a single feather for a given species.

In this present study, we investigate the elastic modulus of contour feathers with a varying cross section, using northern

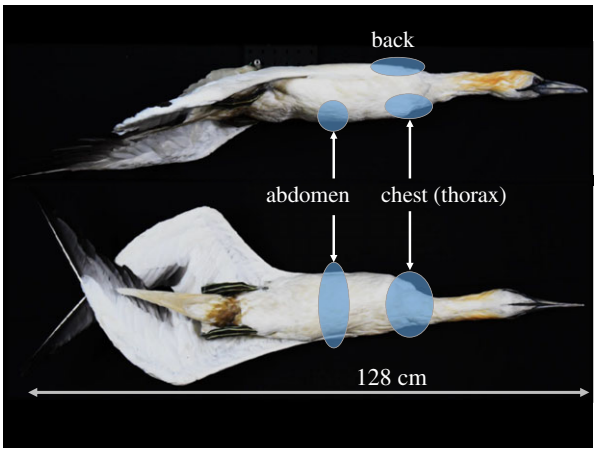


**Figure 2.** Top and bottom image showing the side and ventral view of a northern gannet. Circled regions show the locations from where feathers were plucked, i.e. the abdomen, ventral upper thorax and upper back region. (Online version in colour.)

gannet feathers as a model specimen. Using a point load, the mechanical behaviour of individual contour feathers is quantified under bending load conditions. Young's modulus, $E$, was calculated by correlating bending experimental data on actual feathers with calculations made from the nonlinear bending equation for pre-curved rods while considering the varying area moment of inertia. Thereafter, the role of elastic coupling of feathers in spatial dispersion of force was studied using artificially fabricated elastic beams.

## 2. Material and methods

### 2.1. Materials

#### 2.1.1. Actual gannet feathers

The North Carolina Museum of Natural Sciences, Raleigh, NC, provided two carcasses of salvaged adult northern gannet birds. Both birds were collected and handled under Permits 14-SC00218 and MB575148-0. Carcasses were kept frozen for computed tomography (CT) and feather plucking. One is catalogued at the Smithsonian NMNH under the specimen number USNM 654219 and the other is still being catalogued. The sex is unknown.

Individual feathers were plucked for material characterization. Between seven and ten feathers were randomly taken from each region of interest: abdomen (belly), ventral upper

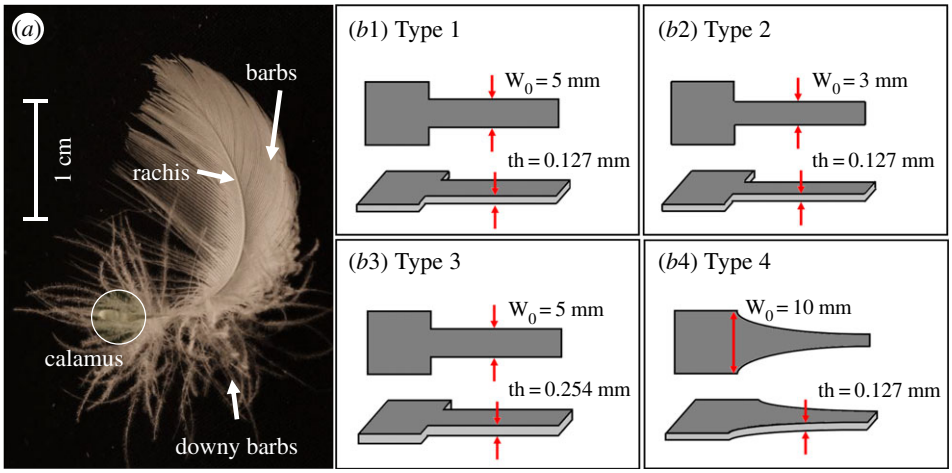


**Figure 3.** (*a*) Northern gannet contour feather (from the chest). The calamus is the thick root of the feather which is clamped by the skin. The calamus eventually tapers into the rachis (which remains above the skin). (*b*) Different configurations of artificial feathers that are used. (*b*1) Thickness = 0.127 mm, length ≈ 20 mm, width = 5 mm. (*b*2) Thickness = 0.127 mm, length ≈ 21 mm, width = 3 mm. (*b*3) Thickness = 0.254 mm, length ≈ 21 mm, width = 5 mm. (*b*4) Thickness = 0.127 mm, length ≈ 22 mm, width = $10 \times \exp(-\Gamma s)$ mm where $\Gamma = 16$ mm$^{-1}$. (Online version in colour.)

thorax, and upper back region (figure 2). Each feather has two main parts: (i) the shaft and (ii) barbs. The shaft is composed of the calamus, which remains embedded in the skin, and the rachis, which is the portion that protrudes outside of the skin (figure 3*a*). Barbs are the thin fibres that branch off of the rachis, which are collectively referred to as vanes. Each barb further branches out into even finer structures called barbules. Barbs that have symmetrical and filamentous barbules, generally found closer to the calamus, are called downy barbs [34,35].

### 2.1.2. Artificial feathers

To understand the coupling effect of feathers in an actual feather patch, we created artificial feathers by using thin elastic beams made of polycarbonate with a pre-curvature, or having a curved shape in an unstressed state. The polycarbonate material used was standard glossy clear polycarbonate sheets; Product# 85585K102 (0.127 mm) and 85585K103 (0.254 mm) from McMaster-Carr Co. The different thickness of sheets give different area moments of inertia. For further variation in the area moment on inertia, the artificial feathers were fabricated in different shapes as well (figure 3*b*). The elastic modulus of the polycarbonate material is measured to be around 1.6 GPa (using the method outlined in §3.3) which is of the same order of magnitude as the known value of around 2.0 GPa [36]. The beams were made by cutting thin strips of the polycarbonate sheets (of thickness 0.127 mm and 0.254 mm) of the desired shapes using a Full Spectrum Laser cutter H-series 20 × 12 or Sihouette Portrait 2. The pre-curvature was achieved by curling the beams around a metal shaft and heating them in an oven at 80°C for a few hours. The beams would then hold their curled shape after removing from the shaft.

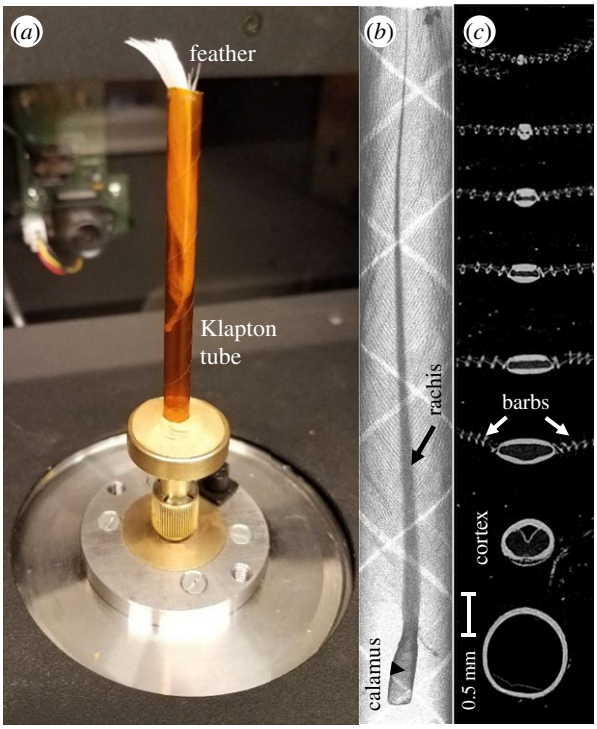


**Figure 4.** (*a*) Feather inside an X-ray invisible tube (Klapton) mounted in the µCT scanner. (*b*) µCT-scanned image of the feather. (*c*) Reconstructed images of feather cross section. The cortex of the rachis is the white, thin-walled structure region. Small white dots that eventually appear to the left and right of the rachis are the barbs and barbules, which are filtered out during image processing. (Online version in colour.)

## 2.2. Methods

### 2.2.1. Micro computed tomography scan

We scanned all feathers using a µCT scanner (Bruker SkyScanner 1173, source voltage 55 kV, source current 110 µA). The slice thickness ranges between 6.1 and 9.09 µm, depending on the size of the feather. Generally, with smaller neck feathers, we obtained a resolution of around 6.1 µm, and larger feathers from the abdomen have a resolution of around 9.09 µm. Each feather was placed inside an X-ray invisible tube (Klapton film tube) during sample rotation. This helped to prevent the feather from moving during scans. After reconstruction, we used Matlab's image-processing toolbox to extract the cross-sectional area of the feather's shaft cortex (the thin-walled region of keratin) along its long axis. In general, the rachis cross section was oval shaped and the calamus cross section was circular shaped (figure 4*c*). During image processing, barbs and barbules that become visible in the µCT scans are subtracted out of the image so that the shaft cortex is the only remaining structure for analysis.

### 2.2.2. Feather characterization

In order to characterize the bending behaviour of a contour feather, Young's modulus was measured using a free-end flexural

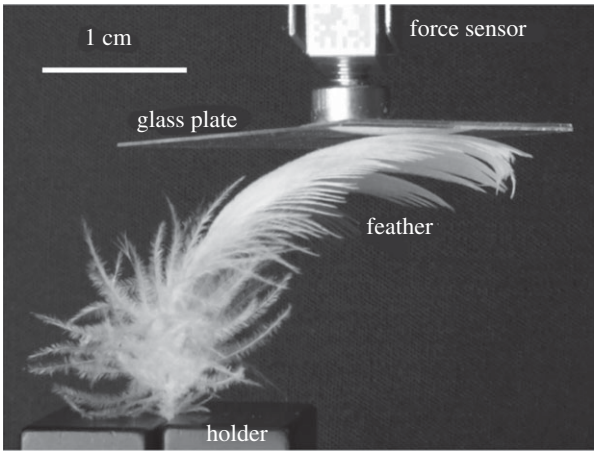


**Figure 5.** Bending test of a single feather. The glass plate and force sensor are lowered vertically and the resulting vertical force is measured. (Online version in colour.)

bending test (figure 5). A small cube was made using vinylpolysiloxane (Zhermack Co., Elite Double 22) with holes on the top surface to clamp the feathers in place. After inserting the calamus into the hole, the base cube was clamped tightly and the bending force of a single feather was then measured. A clear glass plate, attached to a force sensor (Futek LSB200; 10 g) and controlled by a linear stage (Velmex, Inc.), was moved down step-wise, pushing down on the feather rachis. The force data (measured directly by the force sensor) and displacement data (from image analysis using Matlab) result in a force–displacement curve (figure 6).

Initially, for a few feathers, two separate bending experiments were performed. For the first one, the experiment was performed on the whole feather with the vanes intact, while in the second one, similar tests were conducted after cutting off the vanes without disturbing the rachis (figure 6*b*). We see that the results are quite similar (figure 6*a*), leading us to conclude that the resistance of a feather against bending deformation mostly comes from the rachis rather than from vanes. Hence, for subsequent test, the vanes were cut off from the feathers for ease of post-experimental analysis.

Each feather is subjected to a total vertical displacement of around 4.5 mm with three cycles. The resulting force–displacement curves from the three cycles are then averaged.

#### 2.2.3. Multiple feathers: measuring distance between gannet feathers

Bird contour feathers are densely distributed on the skin at about $3.7 \times 10^5$ feathers $m^{-2}$ (for an arc-length and width of about 3 cm and 2 cm, respectively). To measure the distances between feathers, we used the CT-scan slice images to mark the follicles (feather insertions) ($N = 592$) on the feather tracts on the skin (figure 7) using ImageJ (v. 2.0.0). We sampled, at the mid-length of the neck, the dorsal cervical tract and the ventral cervical tract; at the shoulder girdle, the caudal region of the ventral cervical tract and cranial region of the pectorosternal tract as the upper-chest region; the pectorosternal tract as the chest region; and the interclavicular tract as the back region. In cases where the body was too curved for a clear image, several images would compose the sampling for that region. The marking for each feather follicle was used as centre mark for the distance measurements between feathers ($N = 258$). Finally, distances were averaged for each region.

#### 2.2.4. Multiple feathers: physical experiments

The experimental set-up for multiple beams was similar to the single feather experiment, except in this case, we clamp multiple artificial feathers (thin polycarbonate beams) in a linear array with equal spacing between each. This allowed us to precisely control different parameters and measure the resulting force response. We used four different types of artificial feathers as shown in figure 3*b*. The length is chosen to be close to actual feather length ($L_f = 2.5 \pm 0.2$ cm for chest feathers). We carry out experiments with a spacing of 5 mm. Force is again applied to the topmost beam by step-wise pushing it downward with a glass tip attached to a force sensor. The topmost beam presses the succeeding beam below it and, in turn, a cascading effect of force transmission is set up due to the beam pattern (figure 7*b*). Also, another force sensor is mounted at the base of one of the beams in the array.

The force reading from the top force sensor for each step gives the net external impact force on the array of beams, while the reading from the bottom force gives the force at the base of the particular beam where it is placed. The corresponding vertical displacements of each of the beams is measured by image processing using Matlab.

## 3. Results

### 3.1. Area moment of inertia

From the µCT scans, we find that the length of the calamus $L^c$ and rachis $L^r$ varies depending on the region. For the calamus, $L^c_{\text{back}} = 3.5 \pm 0.1$ mm ($N = 7$), $L^c_{\text{belly}} = 5.4 \pm 0.4$ mm ($N = 7$), $L^c_{\text{chest}} = 3.6 \pm 0.5$ mm ($N = 7$), and $L^c_{\text{neck}} = 0.5 \pm 0.1$ mm ($N = 6$). For the rachis, $L^r_{\text{back}} = 24.1 \pm 2.8$ mm, $L^r_{\text{belly}} = 24.9 \pm 0.7$ mm, $L^r_{\text{chest}} = 23.3 \pm 1.5$ mm and $L^r_{\text{neck}} = 6.6 \pm 0.5$ mm. Along the shaft, the cortex's cross section decreases dramatically from the calamus to the rachis, and then slowly tapers to the tip [24,37] (figure 8). The calamus is partly hollow, but the rachis is filled with the medulla. MacLeod [28] measured the feather's mechanical characteristics both with and without the medulla and concluded that it could explain some changes in stiffness along the shaft and between species.

The area moment of inertia, $I$, around the axial direction, i.e. the $y$-axis in this case, was calculated by considering the $z$-plane as the bending plane (figure 10):

$$I = \iint_S y^2_{\text{bend}} \, dx_{\text{bend}} \, dy_{\text{bend}}, \tag{3.1}$$

where $y_{\text{bend}}$ is the direction of bending and $x_{\text{bend}}$ the orthogonal direction for a given cross section $S$.

Experimental values of $I$ for one chest feather are shown in figure 8. From the beginning of the rachis to the tip, the area moment of inertia, $I$, ranges between $10^{-15}$ and $10^{-18}$ $m^4$. Experimental values of $I$ for the back, belly, chest and neck are shown in figure 9*a*. Here, we found that the variation of $I$ along the rachis is significant, which needs to be considered in the analysis. A general trend of decreasing $I$ is observed which allows us to assume a fitting function to describe the $I$'s for chest feathers as shown in figure 9*b*. For the functional form of $I$, we use the non-dimensionalized form of the area moment of inertia (denoted as $I^*(s^*)$), by non-dimensionalizing arc length and area moment of inertia as $s^* = s/L$ and $I^* = I/I_0$, respectively, where $L$ is the rachis length and $I_0 \approx 10^{-15}$ $m^4$ is the area moment of inertia at the base of the rachis:

$$I^*(s^*) = y_1(s^*) \times c_1(s^*) + y_2(s^*) \times c_2(s^*), \tag{3.2}$$

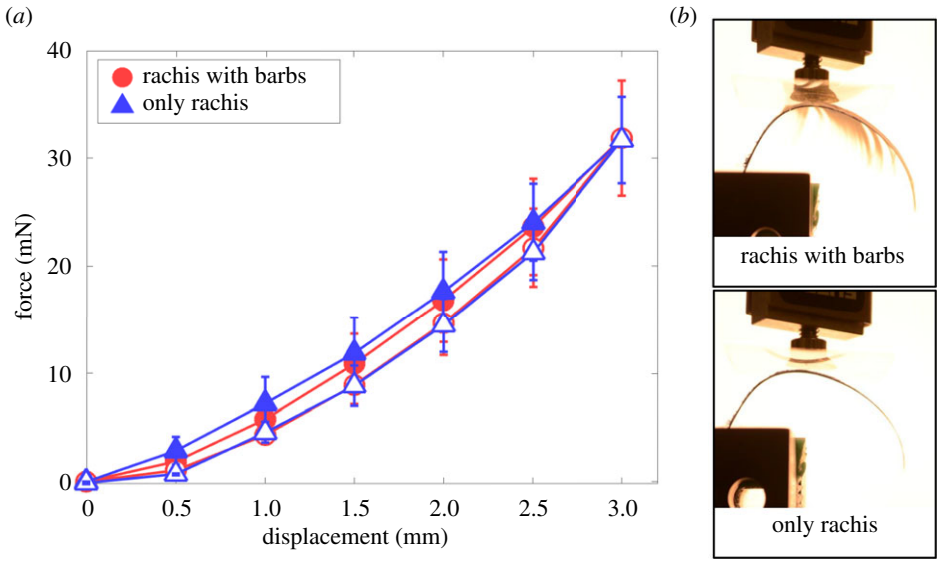


**Figure 6.** (*a*) Force–displacement curves for four different chest feather rachis with and without barbs; the filled data points are for increasing displacements from 0 to 3 mm and the hollow data points are for decreasing displacements from 3 to 0 mm. (*b*) Bending experiment images of one of the feathers with and without barbs. (Online version in colour.)

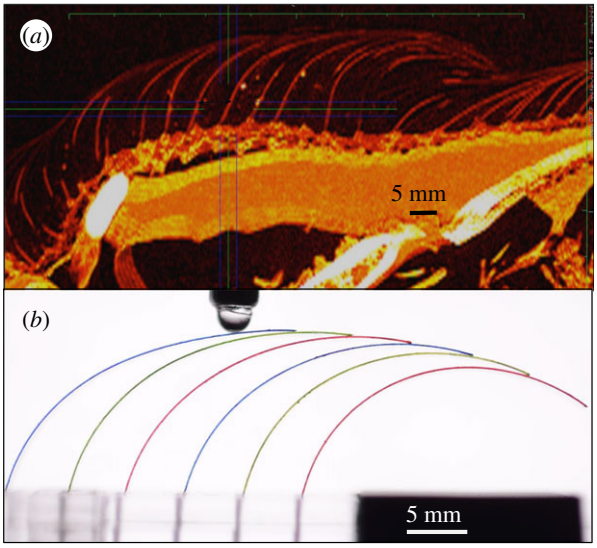


**Figure 7.** (*a*) CT scans of a gannet body showing the two-dimensional feather pattern on the skin. The thin hair-like structures protruding (in bright red) out are the feathers. (*b*) Experimental set-up with artificial feathers (coloured for post-experimental analysis). The sphere at top applying force is attached to the force sensor.

where

$$y_1(s^*) = 0.7\exp(-15s^*) + 0.3,$$

$$c_1(s^*) = \frac{1}{2}(\tanh(-10(s^* - 0.51)) + 1),$$

$$y_2(s^*) = \frac{1}{2}(\tanh(-10(s^* - 0.2)) + 1)$$

and

$$c_2(s^*) = \frac{1}{2}(\tanh(10(s^* - 0.51)) + 1).$$

The constants in the above equations were chosen for the best fit for our experimental data (figure 9*b*).

The range from $s = 0$ to 0.004 m in figure 9*b* represents the calamus part of the feather. Since this part does not affect the bending dynamics of the feather, we ignore it while obtaining the fitted function.

## 3.2. Governing equation for a pre-curved beam

A schematic of the feather in undeformed and deformed shape is shown in figure 10, where $s$ is the dimensional curvilinear arc length axis along the rachis, $F_0$ is the applied point load, $L$ is the arc length of the rachis from the clamp to the point where force is applied, $L_f$ is the total arc length of the rachis, and $\theta$ is the angular deflection from the unstressed position. When the force displaces the feather by $\Delta Y$, the point of contact (or point of load application) also shifts backward relative to the feather by $\Delta L$.

The rachis is modelled as an elastic, homogeneous, isotropic beam, in which the governing equation of this mechanical behaviour is given as [38]

$$\frac{\mathrm{d}}{\mathrm{d}s}\left(EI(s)\frac{\mathrm{d}\theta}{\mathrm{d}s}\right) = -|\boldsymbol{F}_0 \times \hat{t}|, \tag{3.3}$$

where $E$ is Young's modulus (which is assumed to be constant throughout the rachis), $I(s)$ is the area moment of inertia, $\theta$ is the angular displacement caused due to the load $\boldsymbol{F}$ and $\hat{t}$ is the unit vector along the tangential direction of the rachis. The rachis can be assumed to be more or less homogeneous along its length, so $E$ is constant. Slight variations might exist, but such an assumption for simplicity would result in sufficient accuracy for evaluating an average $E$ value for studying the bending properties. This equation is non-dimensionalized by non-dimensional variables $s^*$ and $I^*$. Also, it should be noted that the value of $L$ keeps changing as the feathers are loaded further, i.e. $\Delta Y$ is increased (figure 10). In the unstressed state, the feather has a pre-curvature, which we will denote as $\kappa$. Considering these factors, the final non-dimensionalized equation may be written as

$$\frac{\mathrm{d}^2\theta}{\mathrm{d}s^{*2}} = -\frac{\mathrm{d}I^*/\mathrm{d}s^*}{I^*(s^*)}\left(\frac{\mathrm{d}\theta}{\mathrm{d}s^*}\right) - \frac{\phi}{I^*(s^*)}\sin(\theta + \kappa^* s^*), \tag{3.4}$$

where $\phi = (F_0 L^2)/(E I_0)$ is a non-dimensional parameter which incorporates the force and elastic modulus terms and $\kappa^*$ is the non-dimensionalized pre-curvature, non-dimensionalized as $\kappa^* = \kappa L$. We assume the pre-curvature $\kappa$ to be constant along the entire rachis which is measured through cubic spline fitting

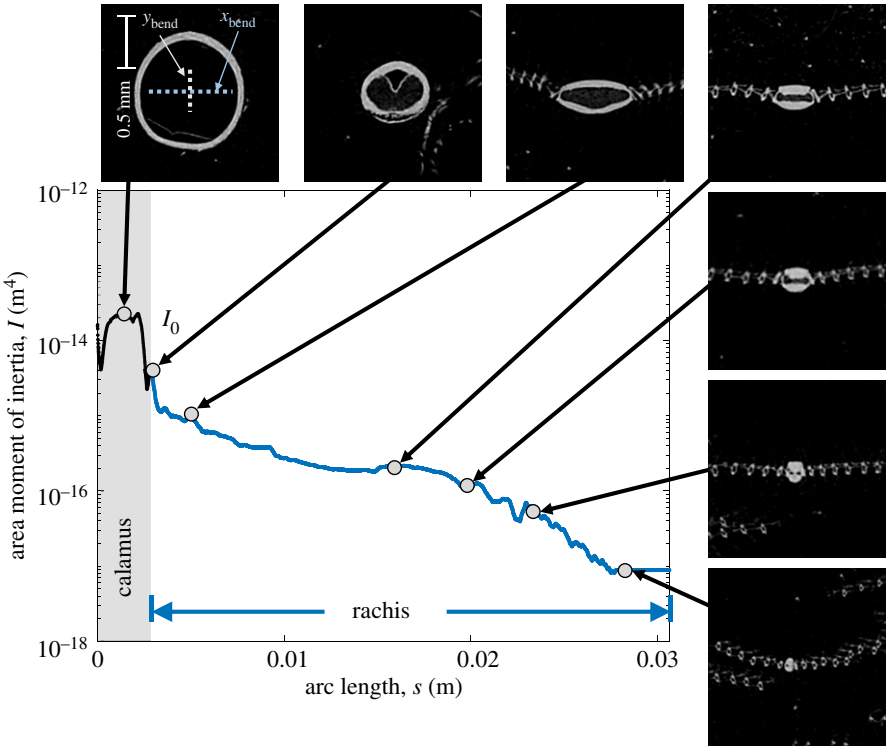


**Figure 8.** Area moment of inertia of the cortex (white thin-walled region) is calculated along the bending axis (horizontal line in frame). X-ray micro-tomography snapshots of a feather shaft and values for $I$ along the arc length, $s$, of the shaft. (Online version in colour.)

of the images of unstressed feathers. The boundary conditions are (i) fixed angle at the base of the rachis $\theta|_{s^*=0} = \theta_0$ and (ii) a torque-free rachis tip $(\mathrm{d}\theta/\mathrm{d}s)|_{s^*=1} = 0$. Here, $\theta_0$ is measured from images taken from experiments. Our theoretical model, unlike previous models [18,19,24,26,28,32], takes into account the pre-curvature and variation in cross section, and is consistent even for large deformations.

## 3.3. Elastic modulus

To calculate the elastic modulus, equation (3.4) is solved numerically using Matlab's bvp4c boundary value problem solver. The solution for $\theta$ is solved for by incrementally increasing the value of $\phi$ (which is a proxy for increasing the applied force). The rectilinear coordinates for the displaced feather are calculated as $x^* = \int \sin(\theta)\,\mathrm{d}s^*$ and $y^* = \int \cos(\theta)\,\mathrm{d}s^*$. Knowing the values of $\phi$ and the resulting solution for $y^*$ allows us to determine the simulation's force-to-$E$ ratio $(F/E)_{\mathrm{sim}} = I_0\phi/L^2$ which gives us a plot of $(F/E)_{\mathrm{sim}}$ versus $\Delta Y$. From experimental data, we get a plot of $F_{\mathrm{exp}}$ versus $\Delta Y$. We compute $E$ values by comparing the two plots at the $\Delta Y$ values from experiments as $E = (F_{\mathrm{exp}}/(F/E)_{\mathrm{sim}})$. Then an average value of $E$ is determined by simply taking mean of all the $E$ values obtained for the different $\Delta Y$ values (as the material of the feather can reasonably be assumed to be homogeneous and hence $E$ should essentially be a constant value over $\Delta Y$).

We initially tested this method on curved beams made of vinylpolysiloxane polymer (Elite Double 22; Zhermack Co.). We get a value of $E = 0.70 \pm 0.05$ MPa from our method which is in close agreement with the value (0.95 MPa) from the previous literature [17]. Thus, our method gives a value with error margin of about 26%. Next, we applied this method on actual feathers. The results for actual feathers are as below.

The calculated mean value for the rachis Young's modulus ($E$) is $4.84 \pm 1.9$ GPa for chest feathers ($N = 7$) and $6.91 \pm 2.9$ GPa for belly feathers ($N = 7$). Recently, Bachmann *et al.* [24] reported a quite similar value for $E$, 5.4 GPa from bending tests, although it refers to flight feathers. Other previous studies reported between 0.05 [28] and 10 GPa [18], which are quite different from our value but still of the same order of magnitude. Detailed comparison is presented in discussion along with figure 14.

## 3.4. Interaction of multiple elastic beams

In the linear array of beams, we solve the bending algorithm for each beam individually, starting from the lowest one and proceeding up to the topmost one, for each step. Ideally, any $i$th beam (where we start numbering from the topmost beam as $i = 1$ and increase downward to $i = n$ as the lowest beam) in the array experiences three forces: one downward force $F_d^{(i)}$ somewhere near the top part of the rachis due to the beam above it while another upward force $F_u^{(i)}$ acts at the tip of the rachis due to the beam below it and finally a force $F_b^{(i)}$ at the base where its is clamped (figure 11*a*). The net result of $F_d^{(i)}$ and $F_u^{(i)}$, denoted by $F_0^{(i)}$ (figure 11*b*), is what causes the bending, while $F_b^{(i)}$ simply balances off $F_0^{(i)}$. $F_u^{(i)}$ and $F_d^{(i)}$ can be related as $F_u^{(i)} = F_d^{(i-1)}$.

To simulate the bending of any $i$th beam in the array, we concentrate on the part from $s = 0$ to $s = L$ only. The two forces on the beam can be effectively represented by just a single force $F_0^{(i)}$ downward and an additional clockwise moment $M_e^{(i)}$, both acting at $s = L$. The value of $M_e^{(i)}$ is given as

$$\boldsymbol{M}_e^{(i)} = \int_{s=L}^{L_f} (\boldsymbol{F}_u^{(i)} \times \hat{t})\,\mathrm{d}s, \tag{3.5}$$

which simplifies to $M_e^{(i)} = |F_u^{(i)} L_m|$ in the clockwise (positive) direction. Now, we can use the same governing equation (3.4) to get a plot of force versus displacement, except with slightly modified boundary conditions. The new normalized boundary conditions used are (i) a fixed angle at the base of rachis

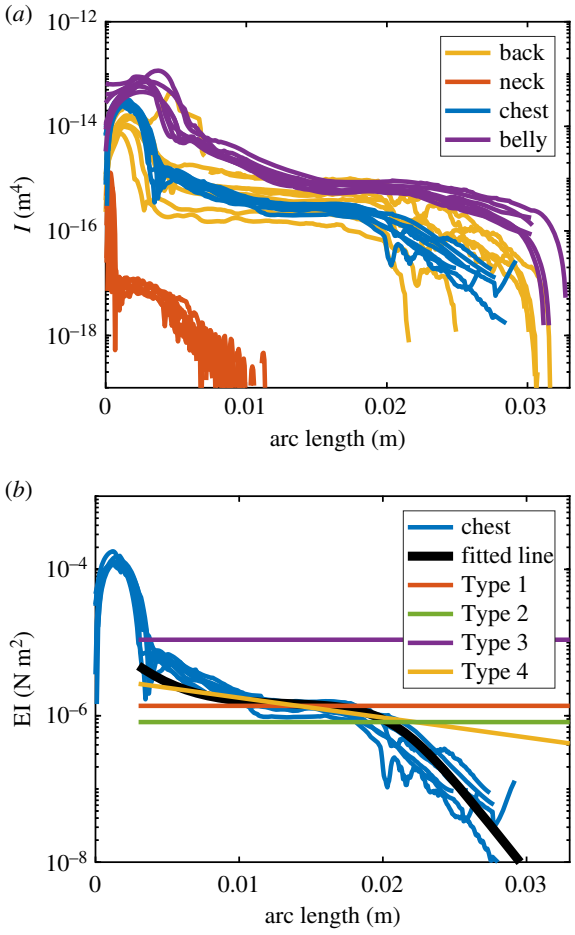


**Figure 9.** (*a*) Area moment of inertia for feathers from the chest, belly, back and neck. In general, neck feathers are shorter and thinner compared to other contour feathers on the body. (*b*) Area moment of inertia of chest feathers is fitted with a double exponential function (black line). Four types of beams we manufactured (figure 3) are plotted for comparison. (Online version in colour.)

$\theta|_{s^*=0} = \theta_0$ and (ii) torque at $s^* = 1$ formulated as $(\mathrm{d}\theta/\mathrm{d}s^*)|_{s=1} = -(F_u^{(i)} L_m L)/(EI_o)$ (from (3.5)). This again gives us a force versus displacement plot by varying the value of $\phi$ over a reasonable range. We evaluate the force value for the actual displacement value (obtained from image analysis) by spline interpolation from the aforementioned plot for the specific beam for the particular step.

However, the interpolated force value represents $F_0^{(n)}$. For the case of the lowest beam (i.e. $i = n$), we can easily see $F_u^{(n)} = 0$ as there is no other beam below it to push upward at the tip. So, $F_d^{(n)} = F_0^{(n)}$. Again, $F_u^{(n-1)} = F_d^{(n)}$, so $F_d^{(n-1)} = F_0^{(n-1)} + F_u^{(n-1)}$. Thus, this process can be repeated for all $i$ to find both $F_u^{(i)}$ and $F_d^{(i)}$ going in reverse from $i = n$ to $i = 1$. Finally, the force at the base of each beam can be evaluated as

$$F_b^{(i)} = F_d^{(i)} - F_u^{(i)}. \tag{3.6}$$

The net external force $F_e$ applied to the beam pattern can be calculated from the simulation result as

$$F_{\mathrm{ext}} = \sum F_b^{(i)}, \tag{3.7}$$

which is also what is experimentally measured using the top force sensor. For validation of our simulation, we match the external force values (for each step) obtained from experiments and simulation (figure 12*a*). Also, we have a second force sensor at the base of one of the beams to directly measure the reaction force (figure 12*b*). This value is also matched with results got from the simulation for that beam as well.

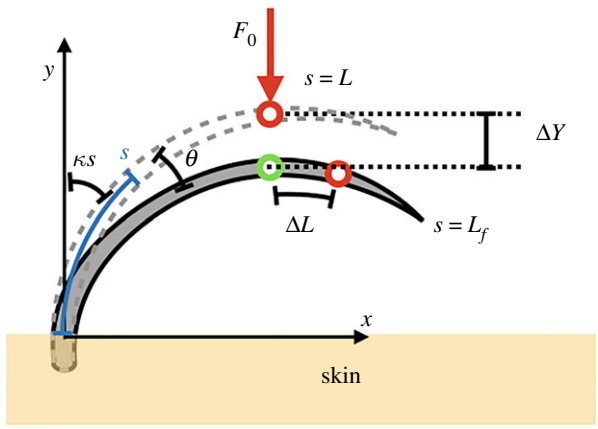


**Figure 10.** Schematic of a pre-curved feather subjected to a point load $F_0$ at $s = L$. The dashed grey line is the profile of the feather in the unstressed state and the solid black line is the equilibrium profile of the feather under load $F_0$. Location of the applied load changes along $s$ (denoted by $\Delta L$) as the feather is deformed. (Online version in colour.)

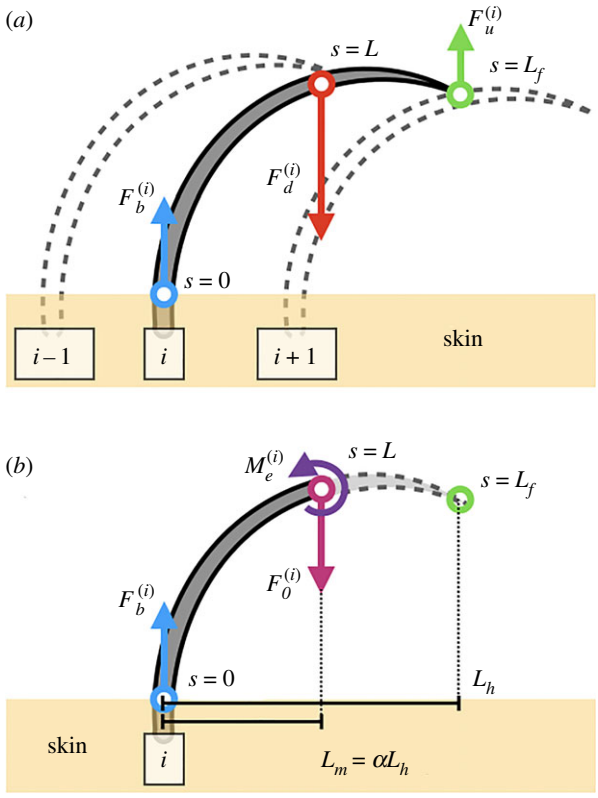


**Figure 11.** (*a*) Schematic of an intermediate beam of interest subjected to two point loads $F_d^{(i)}$ at $s = L$ and $F_u^{(i)}$ at $s = L_f$. The solid black line is the beam of interest and the dashed grey lines are the adjacent beams which exert the forces on this beam. There is additionally a force at the base. (*b*) Part of the beam of interest represented by an equivalent single bending force $F_0^{(i)} = F_d^{(i)} - F_u^{(i)}$ and a moment $M_e^{(i)}$ at $s = L$. (Online version in colour.)

## 3.5. Spreading an impact force

We now turn to the estimation of the spreading of the impact force. Let us consider $n$ feathers organized as in figure 11*a*. Let us assume that an external point force $F_{\mathrm{ext}}$ is applied on the first feather at a horizontal distance $L_m = \alpha L_h$ from the

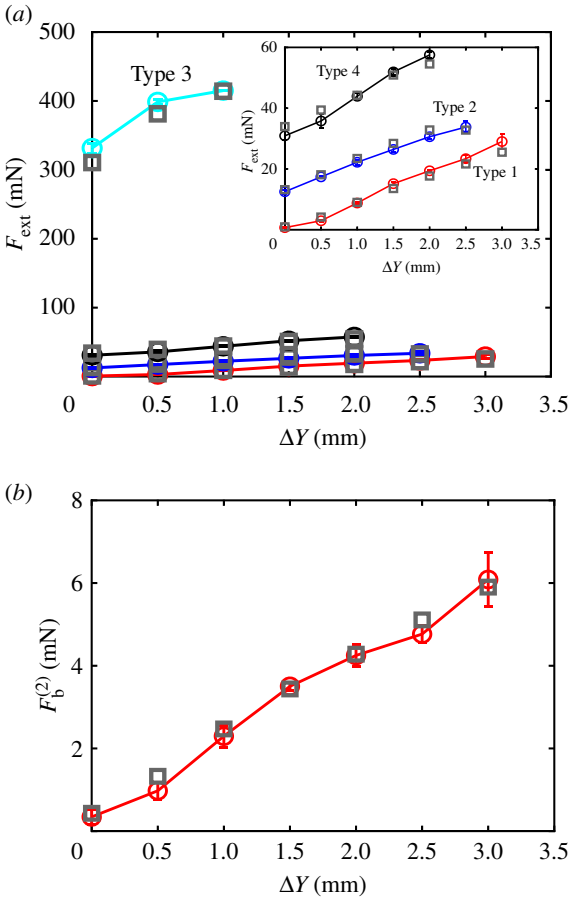


**Figure 12.** (*a*) External force for multiple displacements for all the different types of artificial feathers (circles are for experimental data with errorbar; squares are for simulation results). (*b*) Base force on the second beam from top for Type 1 feathers. (Circles are for experimental data with errorbar; squares are for simulation results). (Online version in colour.)

base, where $L_h$ is the horizontal distance from the base to the tip. Hence, the balance of force and moment at equilibrium leads to

$$F_b^{(1)} - F_{\text{ext}} + F_u^{(1)} = 0 \tag{3.8}$$

and

$$M_0 - \alpha L_h F_{\text{ext}} + L_h F_u^{(1)} = 0. \tag{3.9}$$

We define $M_0$ as the moment acting on the base of the first feather. We have therefore

$$F_u^{(1)} = \alpha F_{\text{ext}} - \frac{M_0}{L_h} \tag{3.10}$$

and

$$F_b^{(1)} = (1-\alpha)F_{\text{ext}} + \frac{M_0}{L_h}. \tag{3.11}$$

On the $n$th feather, we obtain similarly

$$F_b^{(n)} = (1-\alpha)\alpha^{n-1}F_{\text{ext}} + \alpha^{n-1}\frac{M_0}{L_h} \tag{3.12}$$

and

$$F_u^{(n)} = \alpha^n F_{\text{ext}} - \frac{1-\alpha^n}{1-\alpha}\frac{M_0}{L_h}. \tag{3.13}$$

We now derive the number of feathers affected until the force acting on the tip of the feather vanishes, i.e. $F_u^{(n)} = 0$. From equation (3.13), we get

$$n = -\frac{1}{\log(\alpha)}\log\left(1 + \frac{1-\alpha}{M_0/L_h}F_{\text{ext}}\right). \tag{3.14}$$

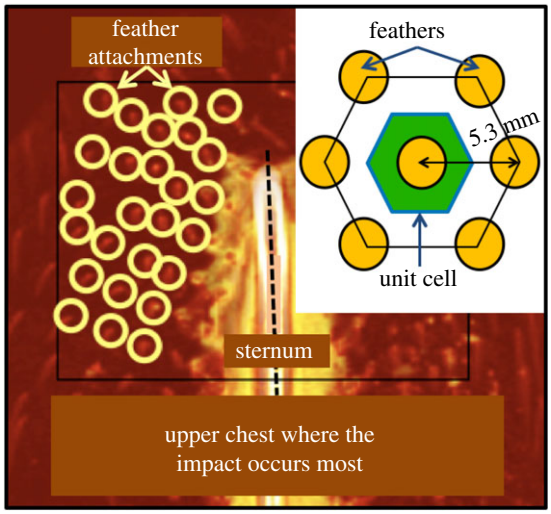


**Figure 13.** Feather attachments in the upper chest of northern gannet. Inset: unit cell is defined as the skin area supporting a single feather. (Online version in colour.)

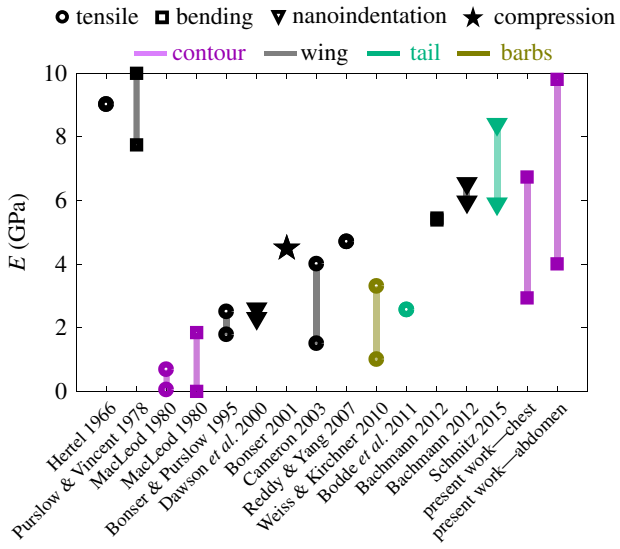


**Figure 14.** Comparison of *E*-values from other works with respect to method of testing (shapes) and feather type. Representative species of the related works are shown in table 1 and their *E*-values are listed in the electronic supplementary material. The last two lines are from the current work with *E*-values from the chest and abdomen. (Online version in colour.)

Here, the parameters can be estimated based on measurements on our feathers $\alpha \simeq 0.685 \pm 0.004$, $L_h = 1.55 \pm 0.07$ cm. The $\alpha$ and $L_h$ values were evaluated simply by measuring the distances on the image using ImageJ. Also, the hydrodynamic pressure due to impact can be estimated as $P_{\text{water}} \simeq (1/2)(\rho_{\text{water}})(\text{Impact speed})^2 \sim 300$ kPa. We estimate the moment from an anatomical perspective [39], assuming that the calamus is maintained straight by muscular forces $F_{\text{Calamus}}$, proportional to the surface of the calamus $S_{\text{Calamus}} \simeq 1\ \text{mm}^2$. Also, muscles are attached at the base of the calamus at a depth of $3.8 \pm 0.5$ mm based on CT-scanned images. Using a typical force density of muscles of $6 \times 10^5\ \text{N m}^{-2}$ [40], we get $F_{\text{Calamus}} \sim 0.6$ N and a moment at the calamus $M_0 \sim 10^{-3}$ N m.

Based on all parameters for actual bird feathers, we expect a spread of the impact force occurs over $n \simeq 9$ feathers, which

is about 4 cm. Furthermore, to illustrate that the spatial spreading of impact force by the presence of feathers actually reduces the pressure on the skin, we define a unit cell as in figure 13, having an area ($S_{cell}$) of 18.24 mm$^2$; and compare the pressure on it both with and without feathers. The force on the feather above the unit cell is $F_{ext} \simeq P_{water} \times S_{cell} \sim 5.4$ N out of which 1.8 N is transferred to the unit cell on the skin as follows from equation (3.11). The corresponding pressure on the unit cell in the presence of a feather is 98 kPa as opposed to 300 kPa without feathers. Thus, feathers on skin can help to spread the impact force over a wide area by reducing the pressure by as much as 3 times in the case of northern gannets.

## 4. Discussion

This study has provided estimates for Young's modulus of northern gannet contour feathers through bending stress tests. The cross-sectional area of the contour feather cortex is found by using a μCT scanner [41]. From these images, we find that the area moment of inertia changes by three orders of magnitude from where the rachis begins to where it ends. The rachis is modelled as an elastic beam, and by numerically solving for the displacement of the beam and comparing the solutions with the experimental force–displacement curves, the average value found of the contour feathers was calculated as $4.84 \pm 1.9$ GPa ($N = 7$).

The advantage of our method is that it accounts for the pre-curvatures and a varying area moment of inertia of the feather in large deformations, which allows us to get an average elastic modulus for the entirety of the structure that undergoes bending. Other works cut their feather samples into pieces, which allow them to apply small deflection bending equations and consider nearly constant values of area moment of inertia ($I$). This allows for calculations of the elastic modulus only in localized regions of the feather. However, previous works have shown some variation of the elastic modulus along the feather rachis [19,30]. Our method is non-destructive (we do not cut the rachis into smaller pieces), and it provides the overall mechanical behaviour of the feather.

While the nonlinear bending equation used in this study has advantages, there are a few assumptions made. Firstly, the nonlinear bending equation assumes purely elastic deformations, meaning that no energy is lost between load being applied and the load being removed, so the force–displacement profile would show a single line between increasing and decreasing loads. However, we know that there is hysteresis in the force–displacement profile for the feather. This is typical of viscoelastic behaviour. Secondly, the bending equation only considers in-plane bending, and thereby neglects possible torsion effects. A second camera that captures any deflections out of plane would help to mediate this experimentally. However, we assume that out of plane deflections are very small compared to in-plane deflections. Thirdly, we assume the feather is a homogeneous material. The calculated area moment of inertia comes from only the cortex of the feather. But the rachis is also made up of some foam material, called the medulla, which may have an additional effect on the elastic modulus. However, previous works do not account for the medulla within the cortex performance *per se* as it appears to have minimal effect on the total resistance force [18,24,42].

**Table 1.** Table of previous works and the tested bird species. Some references do not provide the scientific name of the animal tested, which are marked as unknown.

| reference | species |
|---|---|
| Hertel 1966 | *unknown* |
| Purslow & Vincent 1978 | *Columba livia* |
| MacLeod 1980 | *Larus argentatus* |
| Bonser & Purslow 1995 | *Ardea cinerea* |
| Dawson *et al.* 2000 | *Sturnus vulgaris* |
| Bonser 2001 | *Cygnus olor* |
| Cameron 2003 | swan *unknown* |
| Reddy & Yang 2007 | chicken *unknown* |
| Weiss & Kirchner 2010 | *Pavo cristatus* |
| Bodde *et al.* 2011 | *Ramphastos toco* |
| Bachmann 2012 | *Tyto alba* and *Columba livia* |
| Schmitz 2014 | *Falco peregrinus* and *Columba livia* and *Falco tinnunculus* and *Accipiter nisus* |
| present work | *Morus bassanus* |

Figure 14 shows the comparison of $E$-values from our study with previous literature; water-dwelling birds are marked with icons above their respective publication (though other birds were also tested in those studies). The large variation in $E$-values can be explained by different testing methods, bird species (table 1), and the type of feather used. Generally, Young's modulus for isotropic materials should be the same regardless of the testing method. However, for an anisotropic material like the feather, the direction of load will affect the resulting Young's modulus. Different bird species and feathers may have varying $E$-values depending on their function. It seems that wing feathers may benefit from having higher elastic modulii for flight purposes. It was shown that the elastic modulus for wing feathers increases from proximal to distal end of feathers, but ostriches do not show this trend [43]. Additionally, increasing the humidity in the testing environment shows decreased values in the elastic modulus [26,33].

Since the northern gannet contour feathers undergo bending when they dive into water, we are most interested in the elastic modulus under bending conditions. The closest and most relevant $E$-value from other works to the present study would be MacLeod (1980) [30], which shows an elastic modulus range of 0.002–1.850 GPa for contour feathers under bending tests. His study includes chickens, turkeys, pheasant, and herring gull. For the herring gull, the elastic modulus in bending is actually around 0.022 GPa, which is two orders of magnitude smaller than the average 1.49 GPa obtained for the northern gannet. One factor that may attribute to this difference is the humidity levels. MacLeod maintained a constant humidity level of 60% throughout all his experiments. In the present study, humidity levels were not controlled, but were held during a dry winter season. Since low humidity results in a higher elastic modulus [26,33], this could explain why the elastic modulus is higher in this study compared to MacLeod's study [30]. Future experiments are necessary to

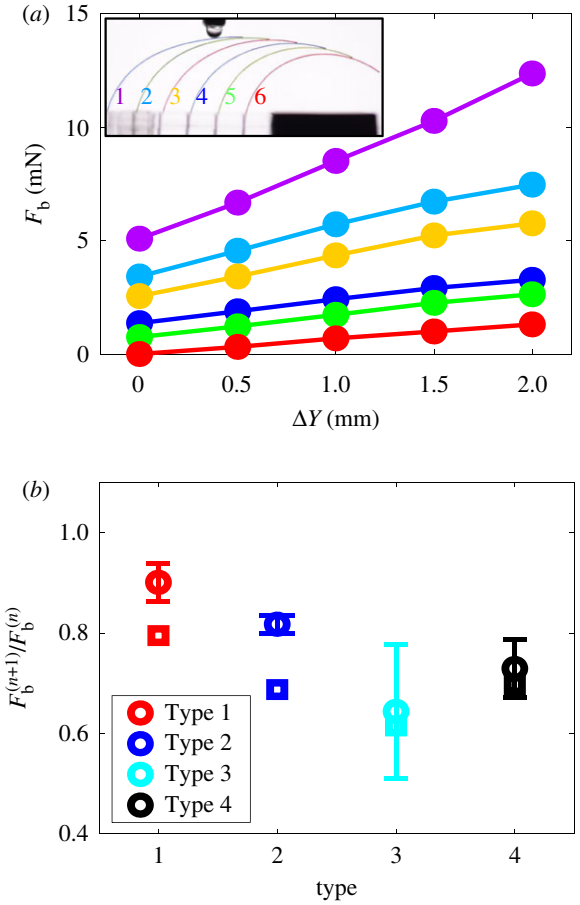


**Figure 15.** (*a*) Forces at the bases (evaluated through simulation) of each beam for Type 2 feathers with 5 mm spacing between each. The steady decline of the forces at the base of feathers as we move away from the application of force can clearly be seen. (*b*) Force distribution ratio at the base for all the feather types (circles are for experimental data with error bar; squares are for theoretical results). The simulation values follow a similar trend to the experimental data across the different types of feathers. However, there is considerable mismatch in the actual values possibly due to the approximation of a zero base moment while computing theoretical values. (Online version in colour.)

test humidity effects on the elastic modulus using the nonlinear bending method presented in this paper.

In order to study the elastic coupling of multiple feathers in an array, we use a similar nonlinear bending model as used for *E*-value calculation. In this case, we have a known *E*-value and use displacements from experiments to compute the forces at all points of every beam one at a time. Thus, we are able to compute the forces at the base of each beam. As seen from figure 15*a*, the net external force applied on the entire patch is borne collectively by all feathers and thus the force experienced on the skin beneath is distributed over a much larger region due to the elastic coupling rather than being more localized as would be expected without elastic coupling of feathers. Thus, we can argue that the presence of feathers on the gannet's skin, particularly around the chest, is likely to have a significant effect on spreading the impact force of water over a much larger area on the skin and in turn minimize the pressure on the chest area, thereby protecting integument. This is under the assumption that a point force arises due to an edge effect at the air–water interface. For example, if a rod of some radius larger than a feather impacts the feather surface, there is pressure that is equal for all feathers within the radius. But outside the radius, or edge, of the rod is where the force begins to dissipate. This can hold true for plunge-diving and many other cases. Such a force-spreading phenomenon would also protect birds from various impacts with solid objects, such as flying into branches, impact with other birds, pecking/fighting, and failed landings on ground and water. However, once a bird is completely submerged underwater, there is no longer a point force, but an equal distribution of pressure acting on the entire body of the bird. An interesting future study is that the collective effect of feathers might actually help maintain an optimal effective stiffness—relatively light or relatively heavy loads do not deform feathers too much—to maintain a specific shape that maximizes trapped air in between the feather and skin, thereby maximizing insulation.

It is worth mentioning that the present work in replicating the elastic coupling in our experiments assumes equilibrium conditions and hence all the force distribution results are subjected to this limitation as well; while the actual bird-diving process is a highly dynamic phenomenon. So, the actual water impact forces are higher in contrast to the experimental forces, but we expect a similar distribution pattern of forces on the bird's skin in nature as illustrated by our study which is our major focus.

Data accessibility. This article has no additional data.

Competing interests. We declare we have no competing interest.

Funding. This research was supported by National Science Foundation grant no. CBET-1604424.

Acknowledgements. The authors thank Dr Carla Dove at Smithsonian Museum of Natural History for helping with specimen dissections, Dr Brian O'Shea at the North Carolina Museum of Natural Sciences for providing specimens and Dr Rolf Mueller at Virginia Tech for use of the micro CT scanner.

## References

1. Herreid II CF, Kessel B. 1967 Thermal conductance in birds and mammals. *Comp. Biochem. Physiol.* **21**, 405–414. (doi:10.1016/0010-406X(67)90802-X)
2. Hausmann F, Arnold KE, Marshall NJ, Owens IPF. 2003 Ultraviolet signals in birds are special. *Proc. R. Soc. Lond. B* **270**, 61–67. (doi:10.1098/rspb.2002.2200)
3. Loyau A, Gomez D, Moureau B, Théry M, Hart NS, Jalme MS, Bennett ATD, Sorci G. 2007 Iridescent structurally based coloration of eyespots correlates with mating success in the peacock. *Behav. Ecol.* **18**, 1123–1131. (doi:10.1093/beheco/arm088)
4. Lentink D, Müller UK, Stamhuis EJ, De Kat R, Van Gestel W, Veldhuis LLM, Henningsson P, Hedenström A, Videler JJ, Van Leeuwen JL. 2007 How swifts control their glide performance with morphing wings. *Nature* **446**, 1082–1085. (doi:10.1038/nature05733)
5. Rohwer S, Ricklefs RE, Rohwer VG, Copple MM. 2009 Allometry of the duration of flight feather molt in birds. *PLoS Biol.* **7**, e1000132. (doi:10.1371/journal.pbio.1000132)
6. Wagner H, Weger M, Klaas M, Schröder W. 2017 Features of owl wings that promote silent flight. *Interface Focus* **7**, 20160078. (doi:10.1098/rsfs.2016.0078)
7. Clark CJ, Elias DO, Prum RO. 2011 Aeroelastic flutter produces hummingbird feather songs. *Science* **333**, 1430–1433. (doi:10.1126/science.1205222)

8. Clark CJ, Elias DO, Prum RO. 2013 Hummingbird feather sounds are produced by aeroelastic flutter, not vortex-induced vibration. *J. Exp. Biol.* **216**, 3395–3403. (doi:10.1242/jeb.080317)
9. Bostwick KS, Prum RO. 2005 Courting bird sings with stridulating wing feathers. *Science* **309**, 736–736. (doi:10.1126/science.1111701)
10. Niese RL, Tobalske BW. 2016 Specialized primary feathers produce tonal sounds during flight in rock pigeons (columba livia). *J. Exp. Biol.* **219**, 2173–2181. (doi:10.1242/jeb.131649)
11. Shiri S, Bird JC. 2017 Heat exchange between a bouncing drop and a superhydrophobic substrate. *Proc. Natl Acad. Sci. USA* **114**, 6930–6935. (doi:10.1073/pnas.1700197114)
12. Ortega-Jiménez VM, Álvarez-Borrego S. 2010 Alcid feathers wet on one side impede air outflow without compromising resistance to water penetration. *Condor* **112**, 172–176. (doi:10.1525/cond.2010.090137)
13. Srinivasan S, Chhatre SS, Guardado JO, Park K-C, Parker AR, Rubner MF, McKinley GH, Cohen RE. 2014 Quantification of feather structure, wettability and resistance to liquid penetration. *J. R. Soc. Interface* **11**, 20140287. (doi:10.1098/rsif.2014.0287)
14. Lee DN, Reddish PE. 1981 Plummeting gannets: a paradigm of ecological optics. *Nature* **293**, 293–294. (doi:10.1038/293293a0)
15. Ropert Coudert Y, Grémillet D, Ryan P, Kato P, Naito Y, Le Maho Y. 2004 Between air and water: the plunge dive of the Cape Gannet *Morus capensis*. *Ibis* **146**, 281–290. (doi:10.1111/j.1474-919x.2003.00250.x)
16. Truscott TT, Epps BP, Belden J. 2014 Water entry of projectiles. *Annu. Rev. Fluid Mech.* **46**, 355–378. (doi:10.1146/annurev-fluid-011212-140753)
17. Chang B, Croson M, Straker L, Gart S, Dove C, Gerwin J, Jung S. 2016 How seabirds plunge-dive without injuries. *Proc. Natl Acad. Sci. USA* **113**, 12 006–12 011. (doi:10.1073/pnas.1608628113)
18. Purslow PP, Vincent JFV. 1978 Mechanical properties of primary feathers from the pigeon. *J. Exp. Biol.* **72**, 251–260.
19. Bonser R, Purslow P. 1995 The Young's modulus of feather keratin. *J. Exp. Biol.* **198**, 1029–1033.
20. Dawson A, Hinsley SA, Ferns PN, Bonser RHC, Eccleston L. 2000 Rate of moult affects feather quality: a mechanism linking current reproductive effort to future survival. *Proc. R. Soc. B* **267**, 2093–2098. (doi:10.1098/rspb.2000.1254)
21. Reddy N, Yang Y. 2007 Structure and properties of chicken feather barbs as natural protein fibers. *J. Polym. Environ.* **15**, 81–87. (doi:10.1007/s10924-007-0054-7)
22. Weiss IM, Kirchner HOK. 2010 The peacock's train (*Pavo cristatus* and *Pavo cristatus* mut. alba) I. Structure, mechanics, and chemistry of the tail feather coverts. *J. Exp. Zool. A* **313**, 690–703. (doi:10.1002/jez.641)
23. Bodde SG, Meyers MA, McKittrick J. 2011 Correlation of the mechanical and structural properties of cortical rachis keratin of rectrices of the Toco Toucan (*Ramphastos toco*). *J. Mech. Behav. Biomed. Mater.* **4**, 723–732. (doi:10.1016/j.jmbbm.2011.01.010)
24. Bachmann T, Emmerlich J, Baumgartner W, Schneider JM, Wagner H. 2012 Flexural stiffness of feather shafts: geometry rules over material properties. *J. Exp. Biol.* **215**, 405–415. (doi:10.1242/jeb.059451)
25. Schmitz A, Ponitz B, Brücker C, Schmitz H, Herweg J, Bleckmann H. 2015 Morphological properties of the last primaries, the tail feathers, and the alulae of *Accipiter nisus*, *Columba livia*, *Falco peregrinus*, and *Falco tinnunculus*. *J. Morphol.* **276**, 33–46. (doi:10.1002/jmor.20317)
26. Wang B, Yang W, McKittrick J, Meyers MA. 2016 Keratin: structure, mechanical properties, occurrence in biological organisms, and efforts at bioinspiration. *Prog. Mater. Sci.* **76**, 229–318. (doi:10.1016/j.pmatsci.2015.06.001)
27. Bonser RHC. 2001 The elastic properties of wing and contour feather keratin from the Ostrich *Struthio camelus*. *Ibis* **143**, 144–145. (doi:10.1111/j.1474-919X.2001.tb04178.x)
28. MacLeod GD. 1980 Mechanical properties of contour feathers. *J. Exp. Biol.* **87**, 65–72.
29. Vincent JFV. 2012 *Structural biomaterials*. Princeton, NJ: Princeton University Press.
30. Macleod GD. 1980 Mechanical properties of contour feathers. *J. Exp. Biol.* **87**, 65–72.
31. Hertel H. 1966 *Structure form movement*. New York, NY: Reinhold.
32. Bonser RHC. 2001 The mechanical performance of medullary foam from feathers. *J. Mater. Sci. Lett.* **20**, 941–942. (doi:10.1023/A:1010993219791)
33. Taylor AM, Bonser RHC, Farrent JW. 2004 The influence of hydration on the tensile and compressive properties of avian keratinous tissues. *J. Mater. Sci.* **39**, 939–942. (doi:10.1023/B:JMSC.0000012925.92504.08)
34. Lucas AM, Stettenheim PR. 1972 Avian anatomy: integument, volumes I and II. Agriculture Handbook 362.
35. Dove CJ. 1997 Quantification of microscopic feather characters used in the identification of North American plovers. *Condor* **99**, 47–57. (doi:10.2307/1370223)
36. Kunori T, Geil PH. 1980 Morphology-property relationships in polycarbonate-based blends. I. Modulus. *J. Macromol. Sci. B: Phys.* **18**, 93–134. (doi:10.1080/00222348008241375)
37. Bostandzhiyan SA, Bokov AV, Shteinberg AS. 2008 Flexural characteristics and aerodynamic aspects of the design of the bird feather shaft. *Dokl. Phys.* **53**, 476–479. (doi:10.1134/S1028335808090036)
38. Landau LD, Lifshitz EM. 1959 *Course of theoretical physics: theory of elasticity*, vol. 7, 3rd edn. Oxford, UK: Butterworth-Heinemann.
39. Homberger DG, De Silva KN. 2003 The role of mechanical forces on the patterning of the avian feather-bearing skin: a biomechanical analysis of the integumentary musculature in birds. *J. Exp. Zool. B* **298**, 123–139. (doi:10.1002/jez.b.30)
40. Ikai M, Fukunaga T. 1968 Calculation of muscle strength per unit cross-sectional area of human muscle by means of ultrasonic measurement. *Int. Z. Angew. Physiol.* **26**, 26–32. (doi:10.1007/bf00696087)
41. Laurent CM, Palmer C, Boardman RP, Dyke G, Cook RB. 2014 Nanomechanical properties of bird feather rachises: exploring naturally occurring fibre reinforced laminar composites. *J. R. Soc. Interface* **11**, 20140961. (doi:10.1098/rsif.2014.0961)
42. Bonser RHC. 1996 The mechanical properties of feather keratin. *J. Zool.* **239**, 477–484. (doi:10.1111/j.1469-7998.1996.tb05937.x)
43. Cameron GJ, Wess TJ, Bonser RHC. 2003 Young's modulus varies with differential orientation of keratin in feathers. *J. Struct. Biol.* **143**, 118–123. (doi:10.1016/S1047-8477(03)00142-4)